Solid State Communications 397 (2025) 115831

Contents lists available at ScienceDirect

Solid State Communications

journal homepage: www.elsevier.com/locate/ssc

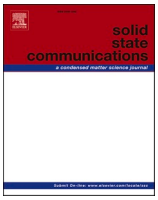

Stability, mechanical, optoelectronic and thermoelectric behaviors of inorganic metal halide double perovskites *(Cs$_2$, K$_2$, Rb$_2$)SnCl$_6$*: Promising green energy alternatives

M.A. Ghebouli [a,b], K. Bouferrache [c], Faisal Katib Alanazi [d,**], B. Ghebouli [e], M. Fatmi [a,*]

[a] Research Unit on Emerging Materials (RUEM), University Ferhat Abbas of Setif 1, Setif, 19000, Algeria
[b] Department of Chemistry, Faculty of Sciences, University of Mohamed Boudiaf, M'sila, 28000, Algeria
[c] Department of Physics, Faculty of Sciences, University of Mohamed Boudiaf, M'sila, 28000, Algeria
[d] Department of Physics, College of Sciences, Northern Border University, Arar, 73222, Saudi Arabia
[e] Laboratory for the Study of Surfaces and Interfaces of Solid Materials (LESIMS), University Ferhat Abbas of Setif 1, Setif, 19000, Algeria

ARTICLE INFO

Communicated by Ralph Gebauer

Keywords:
Conductivity
Seebeck
Chemical potential
DFT
Double perovskites

ABSTRACT

Density functional theory calculations were performed on the stability, mechanical, optoelectronic and thermoelectric characteristics for halide double perovskites *(Cs$_2$, K$_2$, Rb$_2$)SnCl$_6$*. This study focuses on the effects of temperature and chemical potential on electrons transport in these materials. Key transport results include maximum Seebeck coefficient of 1500 μVK^{-1} at 300 K, maximum power factor of 2.5 10^{11} Ws^{-1}K^{-2} at 300 K and maximum electrical conductivity (σ/τ)x10^{19} Wm^{-1}K^{-1}s^{-1} of 11, 6 and 9 at 300 K for *(Rb$_2$, Cs$_2$, K$_2$)SnCl$_6$*. High Seebeck coefficient and high electrical conductivity prove the existence of covalent bonding between Cl-3p site and (Cs-6p, K-4S, Rb-5s) states with weak van der Waals type interactions, which is also confirmed by adsorption analysis. The charge transfer is taking place via Cl-3p and (Cs-6p, K-4S, Rb-5s) states between upper valence band and lower conduction band. The estimated power factor offers useful guidelines for tuning and improving the thermoelectric performance. The density of states predicts the n-type conductivity in all compounds which was confirmed from positive value of Seebeck coefficient.

1. Introduction

Research focuses on new materials with significant performance for renewable energy production and which meet the necessary criteria to resolve energy shortages. An ab-initio calculation provides detailed information on inorganic metal halide double perovskites for solar cells and renewable energy. Fully inorganic metal halide double perovskites have received much attention due to their many advantages, such as high stability. However, it is difficult to achieve efficient near-infrared luminescence in these materials [1]. Inorganic metal halide double perovskites*(Cs$_2$, K$_2$, Rb$_2$)SnCl$_6$* are performed as absorbers for solar cells and renewable energy. We see that the movement of the tin and chlorine atoms resides essentially in a translation and a liberation of the rigid *SnCl$_6$* octahedral. The development of white LEDs attracts researchers to determine new efficient white light-emitting materials. Hybrid organic-inorganic metal halide double perovskites with adequate luminescent properties are promising candidates for LED applications [2]. Solid-state lighting technology has developed in the field of inorganic light-emitting diodes (ILEDs), organic light-emitting diodes (OLEDs), and polymer light-emitting diodes (PLEDs) [3–5]. The excellent optoelectronic properties of metal halide perovskites (MHPs) give them potential applications in solar cells [6–8] and LEDs [9–11]. These metal halide perovskites have the stoichiometric formula A_2XCl_6, where *A* is a monovalent organic/inorganic cation, *X* is a tetravalent metal ion and *Cl* is an ordered halide ion which exhibit fruitful structures and good ion tolerance [12–14]. *Rb$_2$SnCl$_6$* has a direct band gap of 2.40 eV near the visible region, depicts high values of Seebeck coefficient and low thermal conductivity, which make it potential candidate for visible light solar cells and ensure its importance for renewable energy [15]. Synchrotron X-ray diffraction measurements and Raman spectroscopy combined with density functional theory calculations show that *Cs$_2$SnCl$_6$* retains its CFC structure up to a pressure of 20 GPa [16]. A

* Corresponding author.
** Corresponding author.
E-mail addresses: Faisal.katib.al@gmail.com (F.K. Alanazi), fatmimessaoud@yahoo.fr (M. Fatmi).

https://doi.org/10.1016/j.ssc.2025.115831
Received 13 November 2024; Received in revised form 1 January 2025; Accepted 6 January 2025
Available online 7 January 2025

general study of stability, some characteristics such as mechanical, optoelectronic and thermoelectric for *(Cs$_2$, K$_2$, Rb$_2$)SnCl$_6$* are explored. The experimental synthesis is done by taking 0.178 g of Sn powder dissolved in 0.125 ml of HCl to obtain a hydrochloric acid solution $SnCl_2$. 0.505 g of *(Cs, K, Rb)Cl* is added to a beaker, 26.5 ml of deionized water and 9 ml of HCl are used to prepare the sample at the reaction condition of 0.042 mol/L reactants and 3 mol/L HCl. Finally, 1.5 mmol of $SnCl_2$ solution is added. The mixture is stirred at room temperature for 7 h, the precipitate is recovered by centrifugation and washed with anhydrous ethanol [17,18]. Thermoelectric measurements such as the Seebeck coefficient, conductivities and power factor in the cases of spin-up and spin-dn allow the understanding of the complex role of electron spin at high temperatures and its role in energy recovery applications [19]. The heteroatom-doped porous carbons are promise for constructing perovskite solar cells and enhance its efficiency and stability [20]. The ideal tolerance factor, the positive frequencies of phonons dispersion and negative formation energies ensure the structural and thermodynamic existence, and dynamic stability of doubles perovskites [21]. Electrical and thermal conductivities, Seebeck coefficient and power factor explain the thermoelectric analysis for energy applications [22]. The importance of halide perovskite NCs is noted in optoelectronic applications, including light-emitting devices (LEDs), solar cells, lasers, thin film transistors (TFTs) [23]. Perovskite solar cells (PSCs) are gaining popularity due to their high efficiency and low-cost fabrication [24]. Halide perovskites have been a hot topic in electronic medical equipment, and medical stents [25]. We optimized the lattice constant of *(Cs$_2$, K$_2$, Rb$_2$)SnCl$_6$* in the simple cubic phase with space group $Fm\bar{3}m(225)$. The result reveals that these double perovskites are suitable for solar cells and optoelectronic devices. The stability of these materials is ensured by the study of the optimization energy and the phonon spectra. Our optical parameters results indicate that optimal light absorption is in the infrared (IR) region, reflecting the use of these metal halides double perovskites in optoelectronic devices. The transport characteristics are examined in terms of figure of merit, electrical conductivity, thermal conductivity and Seebeck coefficient. Our results are useful for future experimental research for applications related to renewable energy devices. The Wien2k code has been compiled based on the FP-LAPW method, which has the best performance as compared to other codes. Perovskite-based cells are a new generation of photovoltaic cells, which have significant efficiency and manufacturing costs. The choice of these materials is their high light absorption, large charge carrier diffusion length and low number of crystal defects.

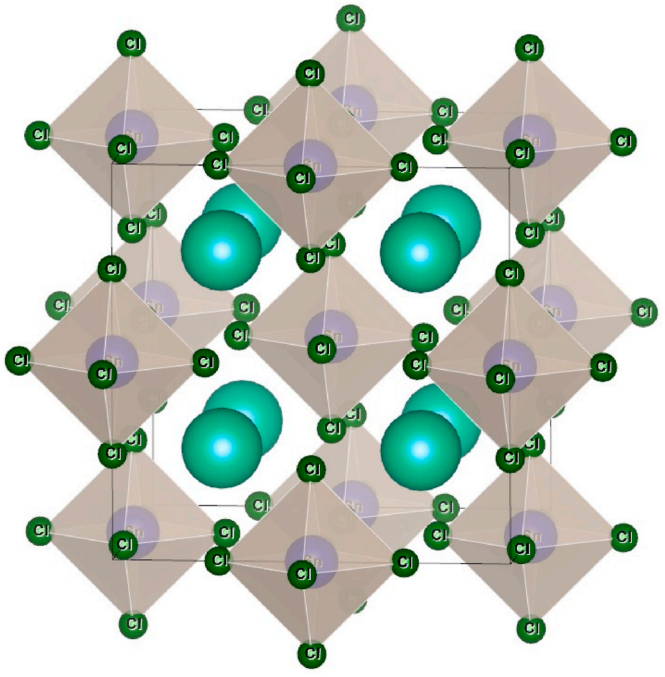

Fig. 1. The cubic crystal structure of *(Cs$_2$, K$_2$, Rb$_2$)SnCl$_6$*, Cl atom (green color), (Cs, K, Rb) (sky blue color) and Sn (grey color).

2. Calculation method

The WIEN2k code is a reliable and precise method in the calculation of stability, mechanical, optoelectronic, and thermoelectric properties [26]. WIEN2k is a powerful computational tool based on the Full-Potential Linearized Augmented Plane Wave (FP-LAPW) method. It offers high precision for solving density functional theory (DFT) equations. Its advantages include accurate band gap with the mBJ-GGA exchange potential, precise structural optimization using GGA-PBESOL, and flexibility in studying a wide range of material properties, such as electronic, optical, thermoelectric, and mechanical characteristics. We introduce the Kohn-Sham Equation:

$\left[-\frac{\hbar^2}{2m}\nabla^2 + V_{eff}\right]\psi_i(r) = \varepsilon_i\psi_i(r)$, where, V_{eff} is the effective potential, combining the external, Hartree, and exchange-correlation potentials. The exchange-correlation GGA-PBESOL and mBJ-GGA functionals are used to improve structural and electronic property predictions. The Birch-Murnaghan equation of state is used for structural optimization:

$$E(V) = E_0 + \frac{9V_0BB_0}{16}\left\{\left[\left(\frac{V_0}{V}\right)^{2/3} - 1\right]^3 B_0' + \left[\left(\frac{V_0}{V}\right)^{2/3} - 1\right]^2\left[6 - 4\left(\frac{V_0}{V}\right)^{2/3}\right]\right\}$$

where $E(V)$ is the energy as a function of volume, V_0 is the equilibrium volume, B_0 is the bulk modulus, and B_0' is its pressure derivative. The Boltzmann transport equation is used for calculating the Seebeck coefficient, electrical conductivity and thermal conductivity.

$$S = \frac{1}{eT}\frac{\int \sigma(E)(E-\mu)f(E)dE}{\int \sigma(E)f(E)dE}$$

where σ(E) is the energy-dependent electrical conductivity, μ is the chemical potential, and $f(E)$ is the Fermi-Dirac distribution. These equations enhance the transparency and reproducibility of the methodology, provide a theoretical foundation for the results and show how computational methods are mathematically grounded. The optimization of the lattice constant was carried out using the GGA-PBESOL approximation [27] which provides a precise value of the lattice constant, but underestimates the band gap. The band structure is a crucial parameter for the electronic and transport properties, therefore, the most accurate mBJ-GGA is used as exchange potential for self-consistency approximation for optoelectronic and thermoelectric properties [28]. We used the value of $R_{MT}.K_{max} = 9$ Ry, where R_{MT} and K_{max} are the muffin-tin radii and wave vector in reciprocal space for *(Cs$_2$, K$_2$, Rb$_2$)SnCl$_6$*. The value of k-points is adjusted as 18x18x18, which was changed to 22x22x22 before computing the transport properties. The lattice constant is optimized using Birch-Murnaghan's equation of state [29]. The R_{MT} of K, Cs, Rb and Sn is 2.5. While the R_{MT} of Cl in K_2SnCl_6, Cs_2SnCl_6 and Rb_2SnCl_6 is 2.15, 2.16, 2.16 respectively. The optical properties are calculated using the Full Potential Linearized Augmented Plane Wave method implemented in the WIEN2k code known for its precision in solving the Kohn–Sham equations. The dielectric function was determined within the random phase approximation. GGA-PBE and mBJ-GGA potentials were used to improve the accuracy of the electronic structure and the derived optical parameters. The real and imaginary parts of the dielectric function, the refractive index, absorption coefficient, reflectivity, and energy loss function were computed as a function of photon energy by employing a dense k-point mesh (18 × 18 × 18) to ensure energy convergence. For the thermoelectric properties, the Boltzmann transport theory was applied using the BoltzTraP2 code. The Seebeck

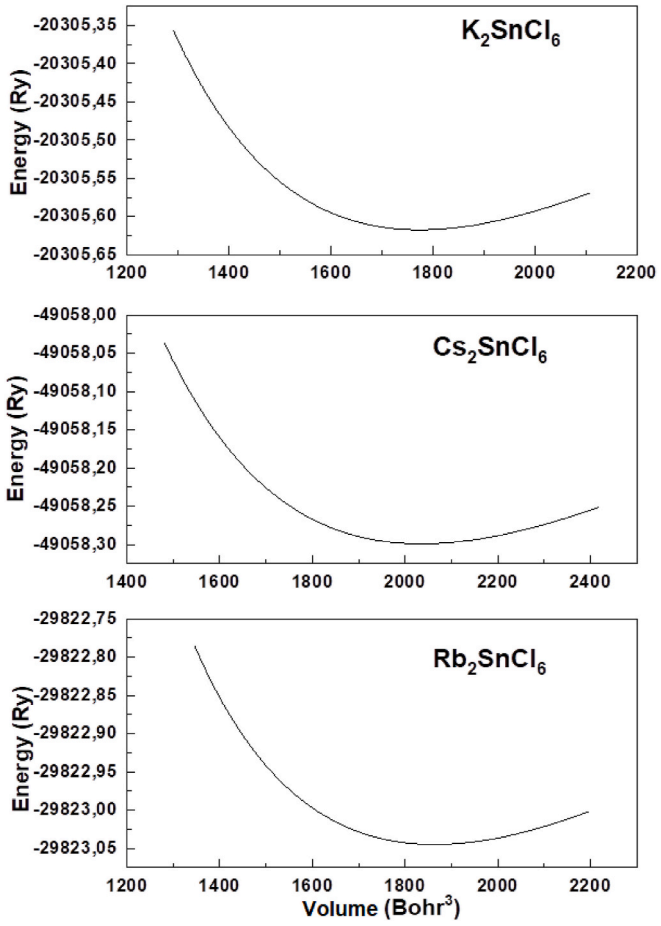

Fig. 2. Optimization energy as a function of volume for *(Cs₂, K₂, Rb₂)SnCl₆*.

coefficient, electrical conductivity, and electronic thermal conductivity were calculated as functions of the chemical potential and temperature. The dense k-point mesh (22 × 22 × 22) sampling ensured the accuracy of energy-dependent transport properties, while the temperature range of 300 K–900 K was explored to capture the thermoelectric behavior under practical operating conditions. The power factor was calculated by combining the Seebeck coefficient and electrical conductivity, providing insights into the thermoelectric efficiency of the materials. k-points are used in calculations to obtain more precision in electronic, optical and thermoelectric properties by minimizing the calculation cost. k-points of 18 × 18 × 18 was employed for electronic and optical calculations, which was sufficient to achieve convergence for total energy and band gap and related optical parameters. These parameters are highly sensitive to subtle variations in the electronic structure near the Fermi level. For thermoelectric characteristics, such as Seebeck coefficient, thermal conductivity, and electrical conductivity, a denser grid of 22 × 22 × 22 was used to ensure higher accuracy in the calculation of energy derivatives and integrations across the Brillouin zone.

3. Results and discussions

3.1. Structure and stability

The cubic crystal structure of *(Cs₂, K₂, Rb₂)SnCl₆* having a base of four-unit cells is schematized in Fig. 1. *(Cs, K, Rb)*, tin and halogen atoms are designed by green, grey and black colors. The lattice constant and the position of the chlorine ion (u, 0, 0) describe the geometric appearance of the structure. The atomic positions are 8K, 8Cs, 8Rb (0.25, 0.25, 0.25), 4Sn (0, 0, 0) and 24 Cl (0.2407, 0, 0). Fig. 2 shows the effect of lattice volume on optimization energy for *(Cs₂, K₂, Rb₂)SnCl₆* and explains the structural stability of these materials. We report in Table 1 the lattice constant, bulk modulus and its pressure derivative and the minimum energy for these compounds. The minimum optimization energy for *(Cs₂, K₂, Rb₂)SnCl₆* indicates that structural stability is present in the materials under study and it is more pronounced following the sequence *Cs→Rb→K*. The computed lattice constant of *Cs₂SnCl₆* and *K₂SnCl₆* are in good agreement with their experimental values [30,31] quoted in the literature, where the uncertainty is 2.7 % and 1.7 % respectively. The lattice constant of *Cs₂SnCl₆* agrees well with theoretical one [32]. Experimental bulk modulus for Cs_2SnCl_6 is cited [33], showing reasonable agreement. The obtained bulk modulus and its pressure derivative from the Birch-Murnaghan equation of state (EOS) are presented in Table 1.

Table 1
Lattice constant, bulk modulus and its pressure derivative and the minimum energy for *(Cs₂, K₂, Rb₂)SnCl₆*.

	a (Å)	B (GPa)	B′	E_{form} (Ry)
K_2SnCl_6	10.169	31.74	4.92	−20305.61
	Exp. 9.988 [31]			
Cs_2SnCl_6	10.645	27.59	5.01	−49058.29
	Exp.10.3562 [30]	9.21 [33]		
	Cal. 10.6841 [32]	26.96 [32]		
Rb_2SnCl_6	10.195	23.11	6.53	−59321.31

Table 2
Bond lengths of nearest neighbors for *(Cs₂, K₂, Rb₂)SnCl₆*.

Bond	K_2SnCl_6	Cs_2SnCl_6	Rb_2SnCl_6
A − *Sn*	4.403	4.609	4.474
(Å)	4.324 Exp.	4.484 Exp.	
A − *Cl*	3.596	3.767	3.655
(Å)	3.532 Exp.	3.663 Exp.	
Sn − *Cl*	2.45	2.479	2.454
(Å)	2.407 Exp.	2.457 Exp.	

The bulk modulus of *Cs₂SnCl₆* agrees well with theoretical and experimental values [32,33]. There are no experimental and theoretical values of the lattice constant and bulk modulus for *Rb₂SnCl₆*. We list in Table 2 the bond lengths of nearest neighbors for *(Cs₂, K₂, Rb₂)SnCl₆* at equilibrium calculated using optimized and experimental lattice constant. The distances are related to the *(Cs, K, Rb)* radius, then bond lengths of *(Cs₂, K₂, Rb₂)SnCl₆* increases in the sequence *K→Rb→Cs*. The study of the dynamic stability requires the use of phonon band structures and PDOS of *(Cs₂, K₂, Rb₂)SnCl₆* as shown in Fig. 3. No negative frequencies are observed in the spectra, therefore dynamic stability is ensured. The optical mode for frequencies located beyond 0.3 THZ for *K₂SnCl₆* and 0.4 THZ for *(Cs₂, Rb₂)SnCl₆* is mainly due to the vibrations of (K, Cs, Rb) atoms, and two atoms in the unit cell vibrate in an opposite direction. While, the acoustic mode with frequencies below 0.25 THZ for *(Cs₂, Rb₂)SnCl₆* and below 0.3 THZ for *K₂SnCl₆*, are governed by the vibrations of the Cl and Sn atoms in the same direction. The phonon spectrum of $(Cs_2, K_2, Rb_2)SnCl_6$ demonstrates dynamic stability under ambient conditions. Under high pressures, the reorganization of the octahedral framework and changes in crystal symmetry may lead to transitions phases. Similarly, high temperatures could induce softening in certain phonon modes, leading to structural changes, such as transitions from the cubic phase to tetragonal or rhombohedral phases. The formation enthalpy of *(Cs₂, K₂, Rb₂)SnCl₆* corresponding to the reaction of formation of these compounds at room temperature from simple elements in their most stable molecular form follows this reaction:

$$(K, Cs, Rb)SnCl_3 + 2HCl + (K, Cs, Rb)Cl + \frac{1}{2}O_2 \rightarrow (K_2, Cs_2, Rb_2)SnCl_6 + H_2O$$

The formation enthalpy of K_2SnCl_6, Cs_2SnCl_6 and Rb_2SnCl_6 is −3.332

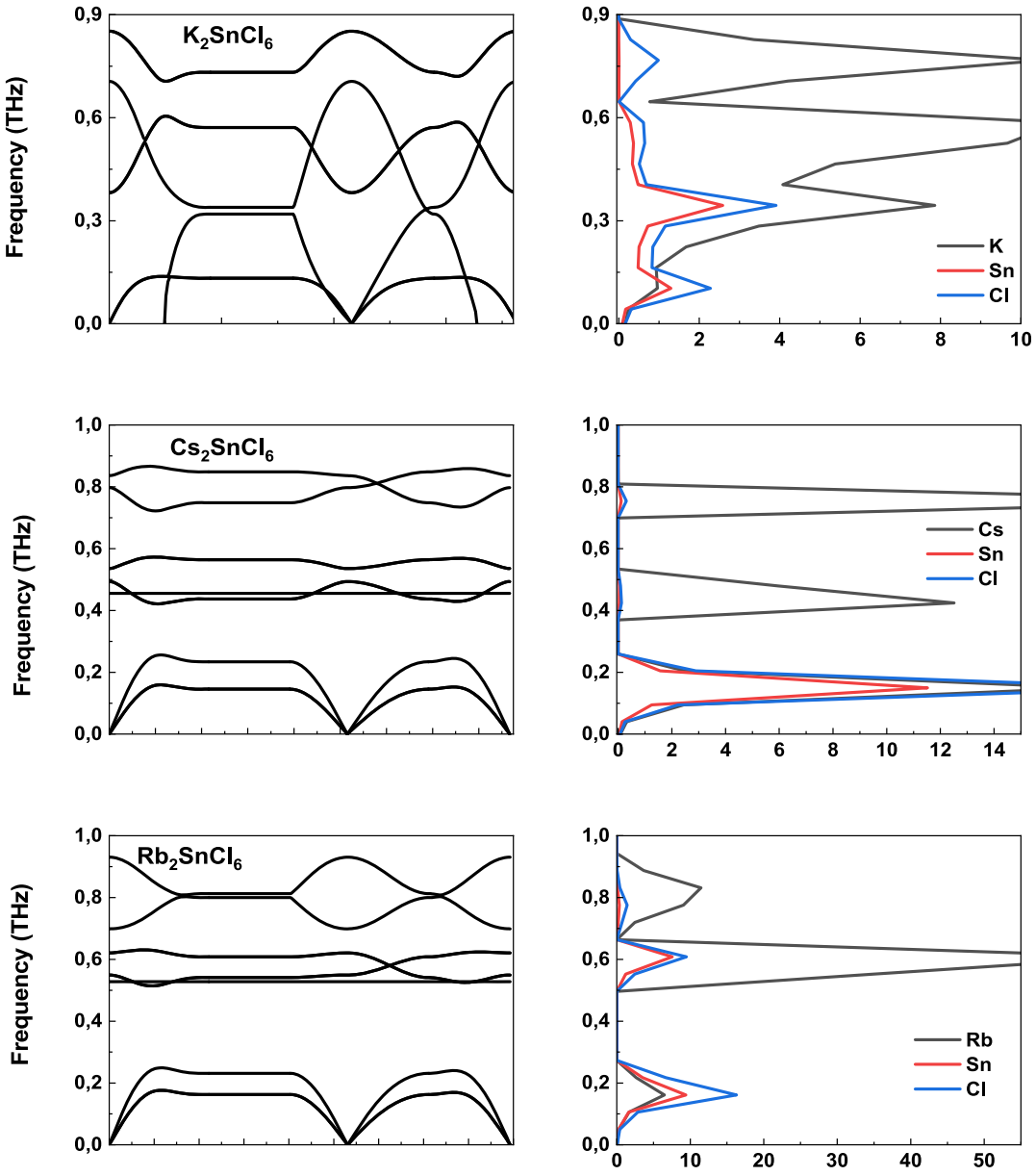

Fig. 3. Phonon band structures and PDOS of *(Cs₂, K₂, Rb₂)SnCl₆*.

Table 3
Goldschmidt's tolerance factor (t), octahedral factor (μ) and ionic radii for *(Cs₂, K₂, Rb₂)SnCl₆*.

	K_2SnCl_6			Cs_2SnCl_6			Rb_2SnCl_6		
Ionic radii (Å)	r_K	r_{Sn}	r_{Cl}	r_{Cs}	r_{Sn}	r_{Cl}	r_{Rb}	r_{Sn}	r_{Cl}
	1.64	0.69	1.81	1.88	0.69	1.81	1.64	0.69	1.81
tolerance factor (t)	0.975			1.044			0.998		
	0.381			0.381					
octahedral factor (u)							0.381		

eV, −3.230 eV and −3.322 eV. The formation enthalpy translates the binding force of a material, and it is the energy needed to dispatch this material into isolated atoms when all the bonds are broken. The negativity of the formation enthalpy of a material reflects its thermal and chemical stability. Goldschmidt tolerance factor (t) and octahedral factor (u) of *(Cs₂, K₂, Rb₂)SnCl₆* as reported in Table 3 are given by $t = \frac{(r_{(K,Cs,Rb)}+r_{Sn})}{\sqrt{2}(r_{Sn}+r_{Cl})}$ [33] and $u = \frac{r_{Sn}}{r_{Cl}}$ [34], where $r_{Sn}, r_{(K,Cs,Rb)}, r_{Cl}$ represent the ionic radii for ions $Sn, (K, Cs, Rb)$ and Cl sites. The double perovskites under study have t and u values close to 1.0 and 0.4, which confirm their structural stability. The synthesis of these materials must be insured their chemical and thermal stability under operating conditions, where we must control the crystal structure, the phase purity and scalability for industrial applications. The stability in the operating conditions of the devices requires their standardized encapsulation. It necessary to focus more on inorganic materials. Optimal design for stable and efficient materials technology includes a thorough fundamental understanding of their structural and photophysical properties under operational

Table 4
The band gap of $(K_2, Cs_2, Rb_2)SnCl_6$ using GGA and mBJ-GGA.

	E_g (eV) GGA	E_g (eV) mBJ-GGA
K_2SnCl_6	2.282	3.726
Cs_2SnCl_6	2.524	3.870
Rb_2SnCl_6	2.312	3.700

conditions. The Goldschmidt tolerance factor for double perovskites under study is close to 1 (ranging from 0.975 to 1.044). This value suggests that the perovskite structure is highly stable for maintaining consistent performance in devices under operational conditions. For optoelectronic application, the structural stability ensures consistent band gap and efficient light absorption and emission. For optoelectronic application, stability is essential for maintaining the low thermal conductivity and high Seebeck coefficient, which are necessary for effective thermoelectric conversion. A structurally stable material ensures reliable charge carrier transport and minimal performance degradation over time.

3.2. Mechanical characteristics

The cubic structure *(Cs₂, K₂, Rb₂)SnCl₆* have three elastic constants and bulk modulus reported in Table 4. Elastic constants and bulk modulus satisfy the stability criteria;

$$C_{11}+2C_{12}\rangle 0, C_{44}\rangle 0, C_{11}-C_{12}\rangle 0, C_{12}\langle B\langle C_{11}$$

which reflect their mechanical stability. Elastic constants are calculated using the stress–strain method, while the bulk modulus of elasticity (B), Young's modulus (E), shear modulus (G), Poisson's ratio (ν) and hardness (H) are calculated with the Voigt–Reuss–Hill (VRH) approximation are reported in Table 4. The weaker elastic moduli lead to their easy deformation and less resistance to stretching or bending and hardness. Young's modulus is the longitudinal modulus of elasticity, which characterizes the resistance of the material to deformation, and the larger the value of Young's modulus, the greater the stiffness of the material. Young's modulus confirms the larger resistance to uniaxial deformation. The values of Poisson's ratio $\nu > 0.25$ support forces as central type in all compounds and the materials exhibit relative toughness. Fig. 4 shows 3D surface of Young's modulus for*(Cs₂, K₂, Rb₂)SnCl₆* double perovskites. It is presented by a contour along each graph in different directions using mBJ-GGA functional. We note that Young's modulus is anisotropic. We study the link between hardness and shear modulus and bulk modulus of double metal halide perovskites calculated according to the model [35]:

$$H = 2\left(\frac{G^3}{B^2}\right)^{0.585} - 3$$

hardness is linked to bulk modulus and shear modulus, which provides information on the resistance of the material to deformation. A higher bulk modulus indicates stronger bonding between atoms, which correlates with greater hardness. A higher shear modulus is associated

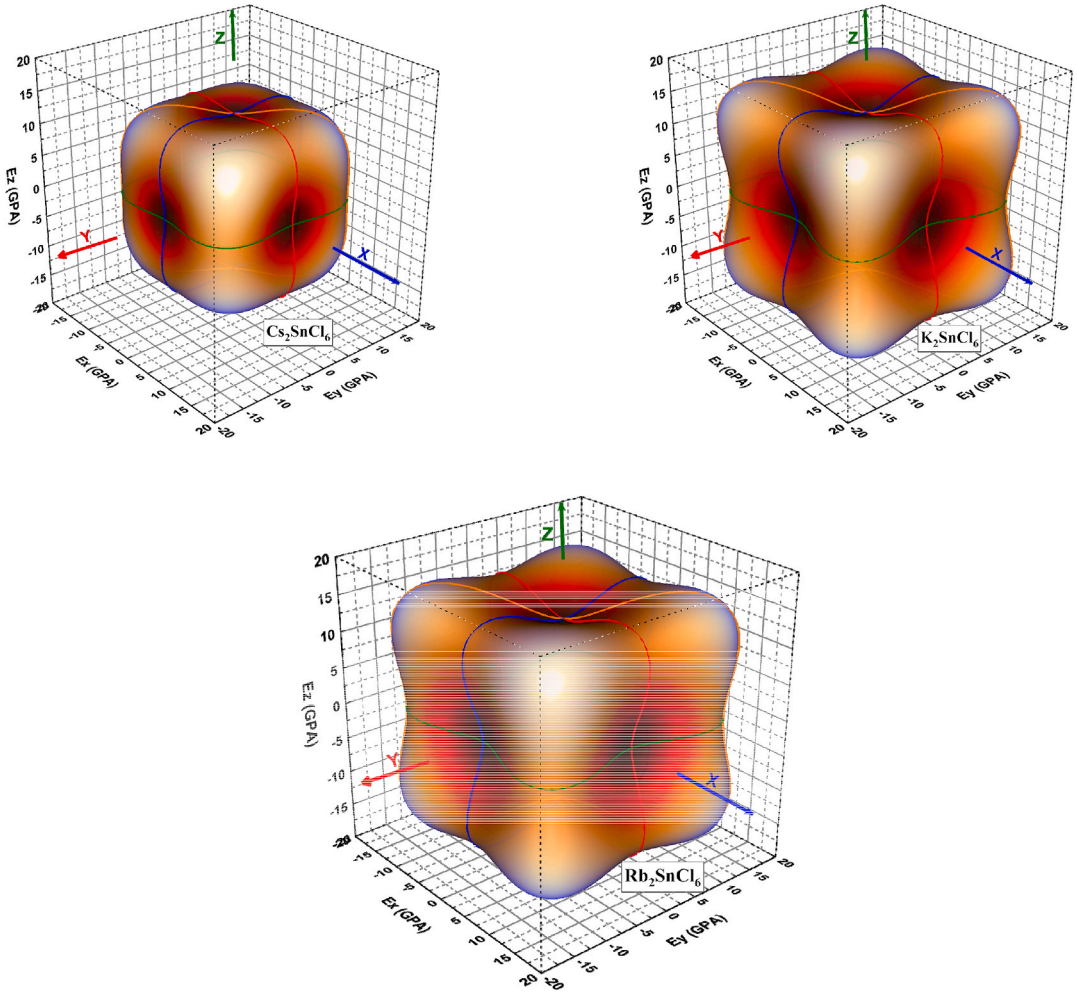

Fig. 4. 3D surface construction of Young's modulus of *(Cs₂, K₂, Rb₂)SnCl₆*.

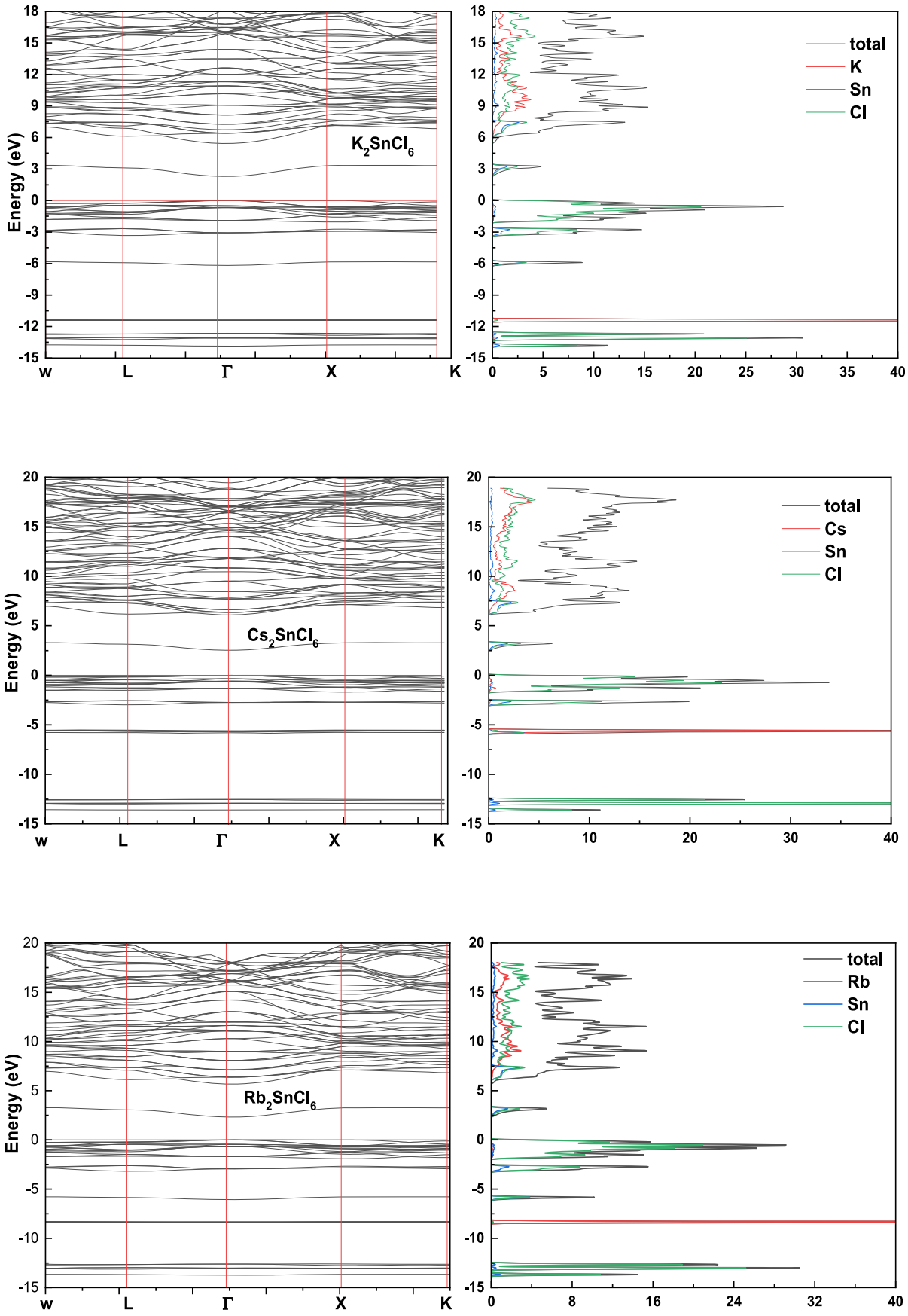

Fig. 5. Electronic band structures and PDOS of *(Cs_2, K_2, Rb_2)$SnCl_6$* using GGA approximation.

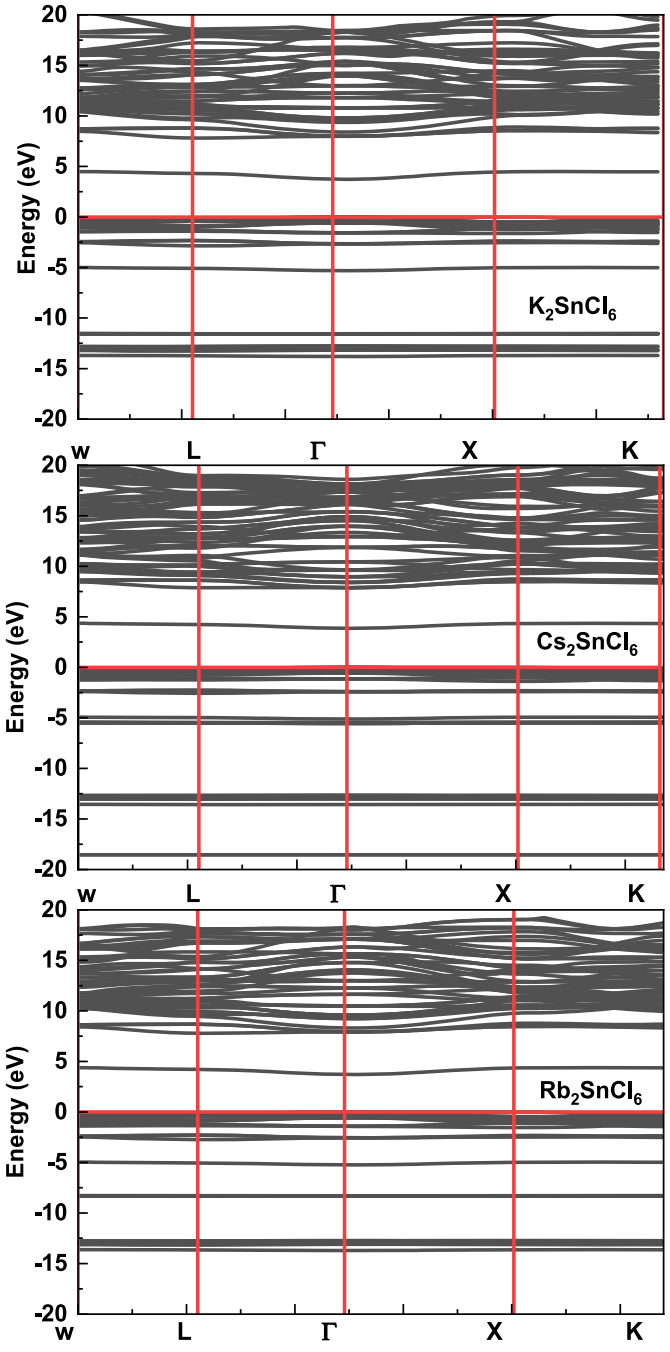

Fig. 6. Electronic band structures of *(Cs₂, K₂, Rb₂)SnCl₆* using mBJ-GGA approximation.

with greater hardness and resistance to plastic deformation. The moderate hardness makes these compounds suitable candidates for reliable and durable device fabrication. There are two independent engineering elastic moduli: the shear modulus (G) and bulk modulus (B). These quantities can be connected to single crystal elastic constants using different averaging techniques. The shear modulus is an indicator of the mechanical hardness. Whereas, the bulk modulus represents a measure of the average bond strength of the atoms in the crystal, and it is proportional to the cohesive energy. The anisotropic nature of Young's modulus suggests that the rigidity of the material varies along the crystallographic axes. The preferred orientation influences the quality of application. Variable stiffness induces a concentration of stresses which have an impact on long-term stability. In thermoelectric applications, preferential orientation improves electron and phonon transport

Table 5
Elastic constants, bulk modulus of elasticity, Young's modulus, shear modulus, Poisson's ratio for *(Cs₂, K₂, Rb₂)SnCl₆*.

		K_2SnCl_6	Cs_2SnCl_6	Rb_2SnCl_6
C_{11} (GPa)		23.35	17.16	22.59
Other cal				
C_{12} (GPa)		13.48	7.54	13.00
Other cal				
C_{44} (GPa)		10.07	7.53	10.85
Other cal				
B (GPa)		16.77	10.75	16.19
Θ_D (K)		181.88	140.41	167.38
Average sound velocity		1857.13	1501.00	1732.90
Bulk modulus	Voigt	16.77	10.75	16.19
	Reuss	16.77	10.75	16.19
	Hill	16.77	10.75	16.19
Shear modulus	Voigt	8.01	6.44	8.42
	Reuss	7.10	6.14	7.20
	Hill	7.56	6.29	7.81
Young modulus	Voigt	20.74	16.11	21.54
	Reuss	18.68	15.47	18.83
	Hill	19.72	15.79	20.20
Poisson Ratio	Voigt	0.293	0.251	0.278
	Reuss	0.314	0.260	0.306
	Hill	0.304	0.255	0.292

performance. The lowest *B*, *G* and *E* values suggest that materials under study are less rigid [36,37]. The large Debye and melting temperatures, hardness and ultralow lattice thermal conductivities increase their importance [38].

3.3. Electronic characteristics

The band structure of *(Cs₂, K₂, Rb₂)SnCl₆* using GGA and mBJ-GGA are presented in Figs. 5 and 6. The Generalized Gradient Approximation underestimates band gap due to its inherent limitations in describing the exchange-correlation energy. The modified Becke-Johnson functional is a more accurate approach for predicting band gap, offering values closer to experimental. The mBJ-GGA functional demonstrates higher accuracy and reliability for band gap prediction, which is crucial for evaluating the suitability of these materials for optoelectronic applications like solar cells and LEDs. Experimental studies confirm the performance of these perovskites in practical devices. The GGA does not accurately describe the discontinuity in exchange-correlation energy, which leads to undervaluing a material's potential in optoelectronic applications. The mBJ-GGA is more accurate and overestimates the band gap slightly, which affect light absorption and charge carrier transport in real-world devices.

It can be seen that valence band maximum and conduction band minimum coincide at the same high symmetry point Γ, which traduce their direct band gap. This addresses one of the main requirements in the manufacturing of energy-efficient solar cells, as well as energy losses in photo-excited electrons due to minimized phonon scattering. We report in Table 4 the direct Γ-Γ band gap of *(Cs₂, K₂, Rb₂)SnCl₆* calculated using GGA and mBJ-GGA functionals. The electronic configuration of Cs, K, Rb, Sn and Cl are Cs: [Xe] $6s^1$, K: [Ar] $4s^1$, Rb: [Kr] $5s^1$, Sn: [Kr] 4 $d^{10}5s^25p^2$ and Cl: [Ne] $3s^23p^5$. The electronic contribution to the first conduction band is mainly due to Cl states. The electronic contribution to the upper valence band is mainly due to Cl-3p states, while the lower conduction band is empty. The charge transfer is taking place via Cl-3p and (Cs-6p, K-4S, Rb-5s) states between upper valence band and lower conduction band. The density of states predicts that all studied double perovskites are n-type semiconductors. We also note that the Cl-p states hybridize with Sn-p-sites, and this confirms that the bonding is covalent in nature. The total density of states (TDOS) clearly shows that the materials under study have a semiconductor nature, because the TDOS of the valence band does not exceed the Fermi level. The presence of an intermediate band in the conduction band of the semiconductors under

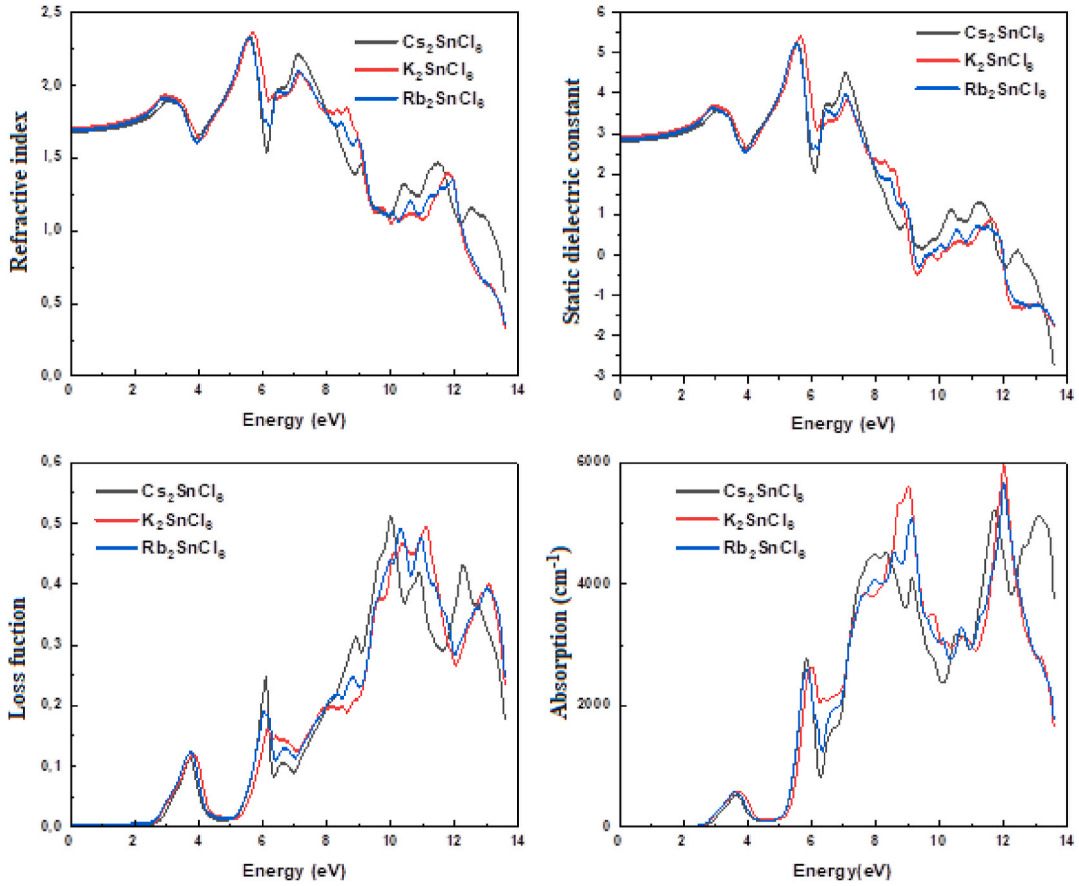

Fig. 7. Refractive index, static dielectric constant, loss function and absorption coefficient as a function of photon energy for *(Cs₂, K₂, Rb₂)SnCl₆* using GGA approximation.

study confirmed by the start of absorption at the photon energy corresponding to the band gap improves the efficiency of these solar cells (Table 5). The intermediate band facilitates the absorption of photons in the sub-band gap and uses low energy photons. This improves the efficiency of solar cells by broadening the absorption spectrum and increasing the photocurrent. Indeed, the band gap of (Cs₂, K₂, Rb₂)SnCl₆ is quite wide, which reduces their effectiveness for applications based on the absorption of visible light, such as conventional solar cells. Fairly wide band gap provides better stability, resistance to photo-induced degradation under harsh conditions. Therefore, these materials are suitable for UV light applications, such as UV LEDs. Therefore, these compounds are useful for specialized applications in other spectral ranges. The hybridization between Cl-p and Sn-p states enhances covalent bonding, stabilizing the crystal structure, contributes to effective charge transport and reduces electron-hole recombination. The perovskites under study are photocatalyst materials because of their suitable structural and electronic characteristics [39]. The examined optoelectronic characteristics of materials under study indicate that they possess promising potential for renewable energy applications [40].

3.4. Optical parameters

The optical parameters studied to illustrate the usefulness of these double perovskites include the refractive index, the static dielectric constant, the loss function, as well as the absorption coefficient are depicted in Fig. 7. The refractive index is an essential parameter in the design of photonic devices. Indeed, the high refractive index is a factor which limits the output efficiency of solar cells. The static refractive index for *(Cs₂, K₂, Rb₂)SnCl₆* is about 1.7. In the visible range, the refractive index is about 3.25. The maximum refractive index observed for these materials is about 5.25, which is observed at the ultraviolet photon energy of 5 eV. Coating with high refractive index materials improves anti-reflective properties and color brilliance, and reduces light loss. Note that the refractive index below 1 in the UV range, traduces that these materials become superluminal. In the propagation of superluminal light, there is a strong dispersion of the refractive index which follows from a strong absorption, this results in a strongly attenuated superluminal light. A superluminal light shows a group velocity greater than that of light in a vacuum, without violating causality. The optical parameters of the double perovskites under study reveal that their optical responses are efficient. The real part specifies the degree of polarization, indicates capacitive or inductive optical response of a material and it is more important in the ultraviolet region. The static dielectric constant $\varepsilon_r(0)$ calculated using GGA for K_2SnCl_6, Rb_2SnCl_6 and Cs_2SnCl_6 is about 2.8. It reaches a maximum value of about 5.4. The large static dielectric constant arises from the lattice contribution and points to the ferroelectric behavior of the material. The materials exhibit large absorption coefficients in the UV range 5500 cm^{-1}, 5000 cm^{-1} and 4500 cm^{-1} for K_2SnCl_6, Rb_2SnCl_6 and Cs_2SnCl_6. The ideal band gap, high dielectric constants and optimal absorption make the double perovskites under study perform well in solar cells. Table 6 lists static dielectric

Table 6
Static dielectric constant, static refractive index and static optical absorption for *(Cs₂, K₂, Rb₂)SnCl₆* using mBJ-GGA.

	ε (0)	n (0)	α (0)
K_2SnCl_6	2,83	1,68	0,0228
Cs_2SnCl_6	2,91	1,70	0,0248
Rb_2SnCl_6	2,86	1,69	0,0242

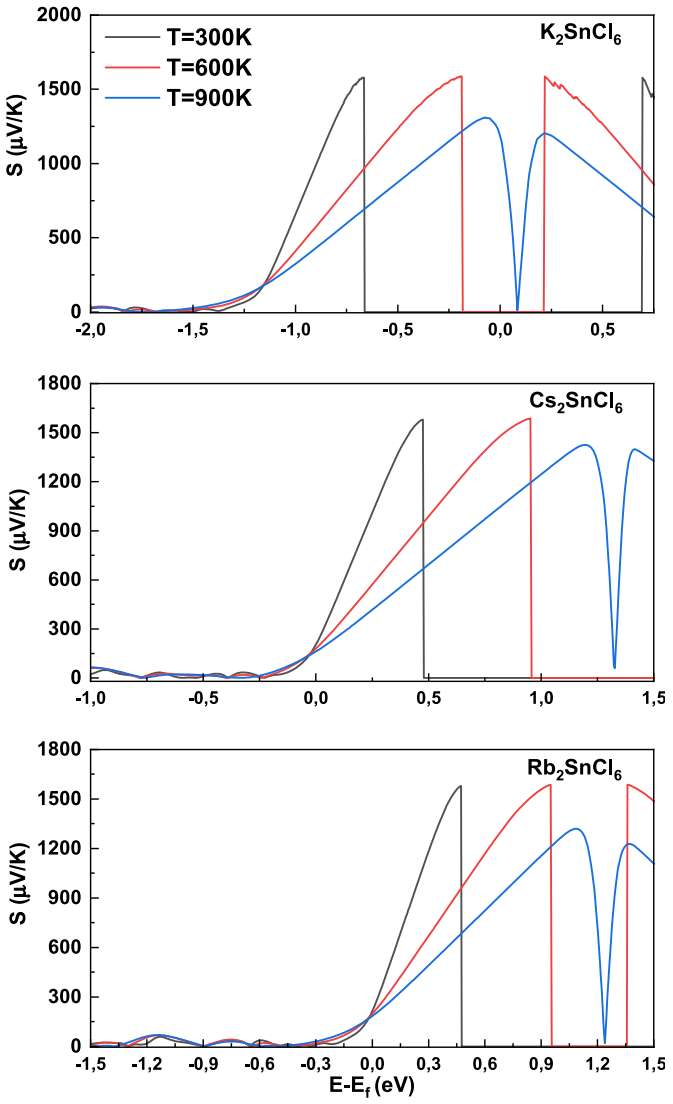

Fig. 8. Seebeck coefficient as a function of chemical potential at temperatures T = 300 K, 600 K and 800 K for *(Cs₂, K₂, Rb₂)SnCl₆* using GGA approximation.

constant, static refractive index and static optical absorption for *(Cs₂, K₂, Rb₂)SnCl₆* using mBJ-GGA. The high absorption and refractive index in ultraviolet light shows their potential in solar energy and thermoelectric devices [41]. The high absorption coefficient at ultraviolet region, high reflectivity near infrared region, the narrow band gap semiconducting nature, high merit factor make the material suitable for optical and thermoelectric applications [42]. A high UV absorption coefficient allows interband transitions and improves photon capture.

3.5. Thermoelectric characteristics

Semiconductors *(Cs₂, K₂, Rb₂)SnCl₆* with direct band gap and flat conduction and valence bands exhibit adequate thermoelectric parameters [43]. Fig. 8 illustrates the effect of chemical potential shifted with respect to the Fermi energy from −1.5 eV to 1.5 eV on Seebeck coefficient at temperatures T = 300 K, 600 K and 900 K for *(Cs₂, K₂, Rb₂)SnCl₆*. Seebeck coefficient increases with increasing chemical potential. The general trend for *(Cs₂, K₂, Rb₂)SnCl₆* with temperature is a decrease in Seebeck. The range of chemical potential increases with increasing temperature. For K_2SnCl_6 two peaks in the profile are observed, the first for n-type character at a chemical potential around -0.6 eV, −0.2 eV and -0.1 eV and the second for p-type character at 0.7 eV, 0.2 eV and 0.2 eV.

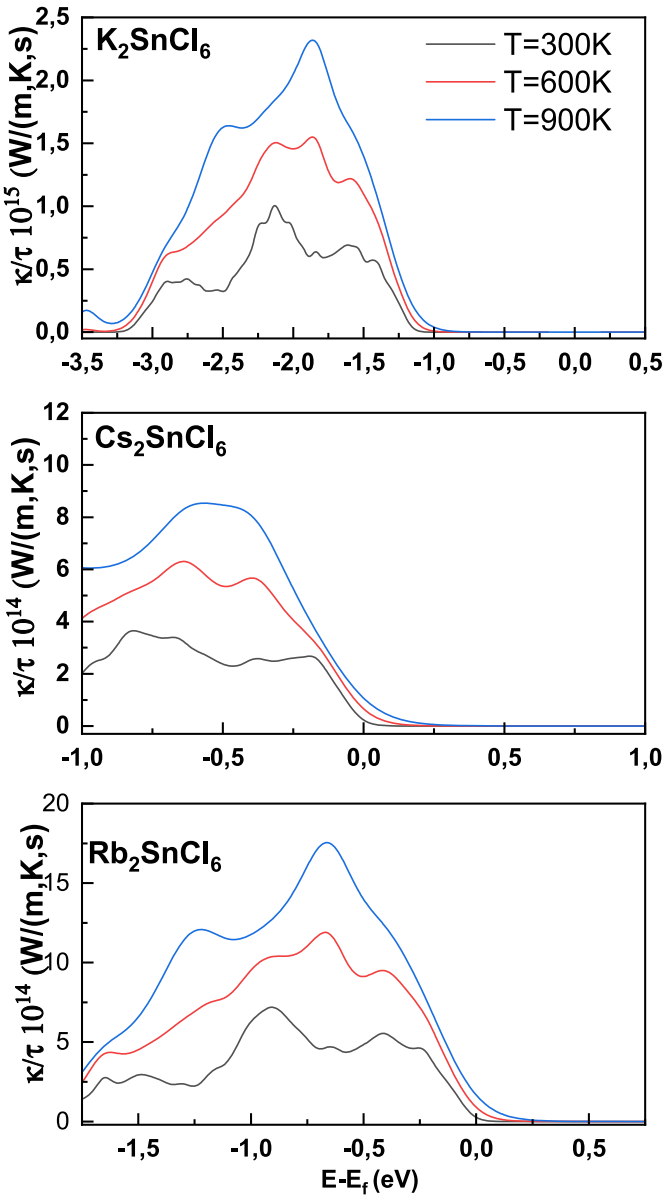

Fig. 9. Electronic thermal conductivity as a function of chemical potential at temperatures T = 300 K, 600 K and 800 K for *(Cs₂, K₂, Rb₂)SnCl₆* using mBJ-GGA approximation.

While *Cs₂SnCl₆* (*Rb₂SnCl₆*) show only one peak at 0.55 eV, 0.95 eV and 1.2 eV (0.45 eV, 1 eV and 1.15 eV) for p-type character. The maximum Seebeck coefficient obtained is about 1500 μVK^{-1} at 300 K and E-E$_F$ = 0.45 eV, 0.5 eV and −0.85 eV for *(Cs₂, K₂, Rb₂)SnCl₆*. We see that *(Cs₂, K₂, Rb₂)SnCl₆* have positive values of Seebeck coefficient which reveals that p-type charge carriers are dominant and increases with increasing temperature for enhancing their performance. The p-type behavior is ensured by positive charge carriers, as confirmed by the positive Seebeck coefficient. The n-type behavior results from asymmetric band structures. At high temperatures, phonon scattering reduces carrier mobility and leads to a reduction in the Seebeck coefficient. Increased thermal excitation equalizes the carrier concentration gradients by limiting the thermoelectric effect. Phonon scattering due to vibrations and lattice defects reduces thermal conductivity and improves thermoelectric performance. Defects act as diffusion centers disrupting heat flow, this maintains a high thermoelectric figure of merit. The thermal conductivity is a combination of electronic thermal conductivity and phononic thermal conductivity. Fig. 9 shows the electronic thermal

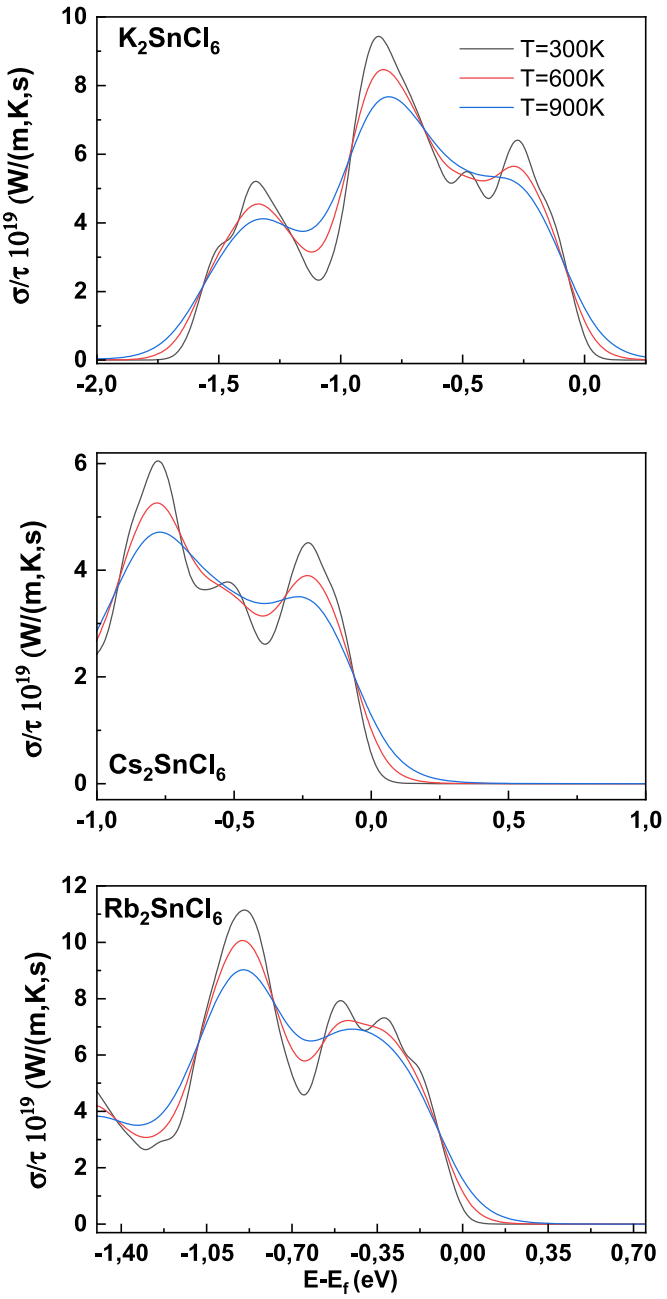

Fig. 10. Electrical conductivity as a function of chemical potential at temperatures T = 300 K, 600 K and 800 K for *(Cs_2, K_2, Rb_2)$SnCl_6$* using mBJ-GGA approximation.

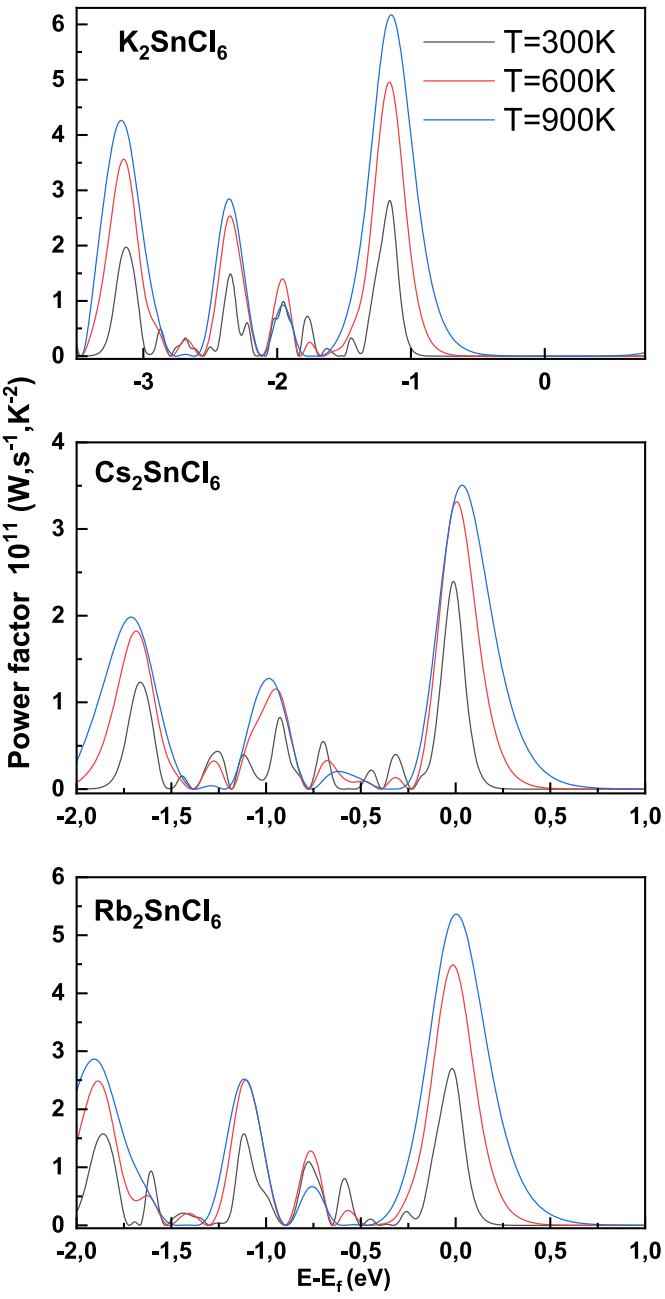

Fig. 11. The power factor as a function of chemical potential at temperatures T = 300 K, 600 K and 900 K for *(Cs_2, K_2, Rb_2)$SnCl_6$* using mBJ-GGA approximation.

conductivity divided by relaxation time as a function of chemical potential at temperatures T = 300 K, 600 K and 900 K for *(Cs_2, K_2, Rb_2)$SnCl_6$*. Thermal conductivity is a parameter for identifying materials intended for technological applications such as thermoelectric conversion. A high-performance thermoelectric material has low thermal conductivity. *(Cs_2, K_2, Rb_2)$SnCl_6$* have positive values of thermal conductivity and this enhances their performance as n-type. Thermal conductivity increases with increasing temperature. Better performance requires the use of low temperature. Thermal conductivity decreases with increasing defects. The dependence of thermal conductivity on temperature in the low temperature region is small. The electronic thermal conductivity enhanced their performance as n-type. Materials under study exhibit competitive Seebeck coefficients and power factors compared to conventional materials. Their thermal conductivity needs to be further optimized to compare performance against state-of-the-art thermoelectrics. The variation of electrical conductivity divided by relaxation time (σ/τ) as a function of chemical potential from −3.5 eV to 1 eV at temperatures 300 K, 600 K and 900 K for *(Cs_2, K_2, Rb_2)$SnCl_6$* using mBJ-GGA is shown in Fig. 10. A high-performance thermoelectric material as n-type has high electrical conductivity, then the use of low temperature. The electrical conductivity for negative chemical potential is higher than that of positive chemical potential. This indicates that the n-type composition possesses higher electrical conductivity than p-type. The average power factor is plotted against the chemical potential at 300 K, 600 K and 900 K as illustrated in Fig. 11. The positive (negative) chemical potential scale indicates the electron (hole) concentration, respectively. The power factor is maximum near $\mu = -1.2$ eV for K_2SnCl_6 and at $\mu = 0$ eV for *(Cs_2, Rb_2)$SnCl_6$*, attributed to significant increment in the electrical conductivity at high electron concentration level. Power factor increases with increasing temperature. The large magnitude of

power factor is obtained in the case of large electrical conductivity. Consequently, *(Cs$_2$, K$_2$, Rb$_2$)SnCl$_6$* exhibit good thermoelectric response at the higher temperatures. The power factor peaks near the chemical potential reflect an optimized carrier concentration. Achieving these conditions requires an adjustment of the Fermi level. Fine-tuning the synthesis parameters and temperature improve the electronic properties, aligning the carrier concentrations to the desired peaks.

4. Conclusion

We used first principles calculations using density functional theory combined with WIEN2k code to perform stability, mechanical, optoelectronic and thermoelectric characteristics. Phonon scattering due to vibrations and lattice defects reduces thermal conductivity and improves thermoelectric performance. The electronic band structure shows that $(K_2, Cs_2, Rb_2)SnCl_6$ have direct band gap semiconductors 3.726, 3.870 and 3.700 eV, with flat valence bands. The flat valence band induces high electrical conductivity, high Seebeck coefficient, excellent values of power factor, which make these materials attractive for thermoelectric applications at high temperature. High absorption coefficient, refractive index and dielectric constants in the ultraviolet light, higher electrical conductivity and lower thermal electronic conductivity and high-power factor make them to be quite suitable for applications in solar cell structures. Bond length plays a key role in material stability, which guides the design of stable optoelectronic semiconductors. The power factor peaks near the chemical potential reflect an optimized carrier concentration.

CRediT authorship contribution statement

M.A. Ghebouli: Formal analysis. **K. Bouferrache:** Formal analysis. **Faisal Katib Alanazi:** Investigation. **B. Ghebouli:** Project administration. **M. Fatmi:** Validation.

Declaration of competing interest

The authors declared no potential conflicts of interest with respect to the research, authorship, and/or publication of this article.

Acknowledgment

The authors extend their appreciation to the Deanship of Scientific Research at Northern Border University, Arar, KSA for funding this research work through the project number NBU-FFR-2025-310-02.

Data availability

No data was used for the research described in the article.

References

[1] J. Sun, W. Zheng, P. Huang, M. Zhang, W. Zhang, Z. Deng, S. Yu, M. Jin, X. Chen, Angewandte 134 (26) (2022) e202201993.
[2] Y. Lin, Y. Zhong, Y. Lin, J. Lin, L. Pang, Z. Zhang, K. Du, Front. Optoelectron. 17 (2024) 6.
[3] J. Shang, C. Cong, Z. Wang, N. Peimyoo, L. Wu, C. Zou, Y. Chen, X.Y. Chin, J. Wang, Nat. Commun. 8 (1) (2017) 543.
[4] A. Kitai, John Wiley & Sons, Ltd (2016).
[5] C.J. Humphreys, Solid-state lighting, MRS Bull. 33 (4) (2008) 459–470.
[6] N. Sun, W. Gao, H. Dong, Y. Liu, X. Liu, Z. Wu, L. Song, C. Ran, Y. Chen, ACS Energy Lett. 6 (8) (2021) 2863–2875.
[7] E.L. Lim, A. Hagfeldt, D. Bi, Energy Environ. Sci. 14 (6) (2021) 3256–3300.
[8] W. Ke, C.C. Stoumpos, M.G. Kanatzidis, Adv. Mater. 31 (47) (2019) e1803230.
[9] K. Zhang, N. Zhu, M. Zhang, L. Wang, J. Xing, J. Mater. Chem. C Mater. Opt. Electron. Devices 9 (11) (2021) 3795–3799.
[10] G. Pacchioni, Nat. Rev. Mater. 6 (2) (2021) 108.
[11] J.S. Kim, J.M. Heo, G.S. Park, S.J. Woo, C. Cho, H.J. Yun, D.H. Kim, J. Park, S. C. Lee, S.H. Park, E. Yoon, N.C. Greenham, T.W. Lee, Nature 611 (2022) 688–694.
[12] S. Liu, B. Yang, J. Chen, D. Zheng, Z. Tang, W. Deng, K. Han, Laser Photon. Rev. 16 (2) (2022) 2100439.
[13] S. Liu, B. Yang, J. Chen, D. Wei, D. Zheng, Q. Kong, W. Deng, K. Han, Angew. Chem. Int. Ed. Engl. 59 (49) (2020) 21925–21929.
[14] A. Abfalterer, J. Shamsi, D. Kubicki, C. Savory, J. Xiao, G. Divitini, W. Li, S. Macpherson, K. Gałkowski, J. MacManus-Driscoll, D. Scanlon, S. Stranks, ACS Mater. Lett. 2 (2020) 1644.
[15] S. Chadli, A. Bekhti Siad, M. Baira, M.B. Siad, A. Allouche, A.B. Reguig, Solid State Commun. 342 (2022) 114633.
[16] G. Bounos, M. Karnachoriti, A.G. Kontos, C.C. Stoumpos, L. Tsetseris, A. Kaltzoglou, X. Guo, X. Lü, Y.S. Raptis, M.G. Kanatzidis, P. Falaras, J. Phys. Chem. C 122 (42) (2018) 24004–24013.
[17] H. Zhang, L. Zhu, J. Cheng, L. Chen, C. Liu, S. Yuan, Crystals 9 (2019) 258.
[18] A.T. Le, T.B. Dinh, T.A. Do, T.G. Ho, D.M. Le, M.T. Man, Mater. Lett. 309 (2022) 131386.
[19] G. Nazir, N.D. Alkhaldi, A. Akrami, J. Hakami, A. Ayyaz, A. Rahman, A.I. Aljameel, M. Jeridi, I. Bukhris, Q. Mahmood, Mater. Sci. Eng. B 310 (2024) 117733.
[20] G. Nazir, H. Liu, A. Rehman, S. Hussain, D. Vikraman, S. Aftab, K. Heo, M. Ikram, A.A. AlObaid, J. Kang, Surface. Interfac. 39 (2023) 102945.
[21] G. Nazir, Q. Mahmood, A. Rehman, A.S. Alofi, H. Albalawi, T. Zelai, O. Hakami, A. I. Aljameel, N. Safina, E. Yousef, J. Phys. Chem. Solid. 184 (2024) 111740.
[22] G. Nazir, Q. Mahmood, T. Zelai, A. Rehman, H. Ablalawi, N.A. Kattan, S. Bouzgarrou, I. Boukhris, Phys. Scripta 99 (5) (2024) 055972.
[23] Y. Mu, Z. He, K. Wang, X. Pi, S. Zhou, iScience 25 (11) (2022) 105371.
[24] R.A. Afre, D. Pugliese, Micromachines 15 (2) (2024) 192.
[25] T.L. Shi, Y.F. Zhang, M.X. Yao, C. Li, H.C. Wang, C. Ren, J.S. Bai, X. Cui, W. Chen, Biomater Transl 4 (3) (2023) 131–141.
[26] K. Bouferrache, L. Krache, M.A. Ghebouli, B. Ghebouli, Sameh I. Ahmed, M. Fatmi, T. Chihi, B. Gueridi, Chemical Physics Impact 5 (2024) 100110.
[27] M.A. Ghebouli, B. Ghebouli, T. Chihi, M. Fatmi, Phys. B Condens. Matter 610 (2021) 412858.
[28] L. Krache, M.A. Ghebouli, B. Ghebouli, S. Alomairy, M. Reffas, M. Fatmi, T. Chihi, Phys. Status Solidi (b) 259 (10) (2022) 2200042.
[29] K. Bouferrache, M.A. Ghebouli, B. Ghebouli, M. Fatmi, H. Bouandas, T. Chihi, Nouf H. Alotaibi, Saikh Mohammad, M. Habila, M. Sillanpää, Mater. Sci. Eng., B 308 (2024) 117550.
[30] B. Thomas, C.R. Gearhart, W.A. Welsh, J. Magn. Reson. 13 (1974) 27–37.
[31] J. Ihringer, Acta Cryst. A36 (1980) 89–96.
[32] K. Bouferrache, M.A. Ghebouli, B. Ghebouli, M.A. Habila, T. Chihi, M. Fatmi, A. Djemli, Mika sillanpaa, Results Phys. 56 (2024) 107138.
[33] U. Ullah, M. Azmat Ali, K.M.S. Katubi, N.S. Alsaiari, K.M. Abualnaja, A.S. Verma, G. Murtaza, Inorg. Chem. Commun. 139 (2022) 109315.
[34] C. Li, K.C.K. Soh, P. Wu, J. Alloys Compd. 372 (2004) 40–48.
[35] Y. Liu, C. Fang, S. Lin, G. Liu, B. Zhang, H. Shi, N. Yang, F. Zhang, X. Guo, X. Liu, Molecules 28 (22) (2023) 7643.
[36] A.I. Aljameel, A. Mera, S. Saad, G. Nazir, H. Albalawi, J. Taibah Univ. Sci. 16 (1) (2022) 155–162.
[37] A.A. Sholagberu, W.A. Yahya, A.A. Adewalee, Phys. Scr. 97 (2022) 085824.
[38] G.M. Mustafa, S. Saba, Q. Mahmood, N.A. Kattan, N. Sfina, T. Alshahrani, A. A. Mera, G.A.M. Mersal, M.A. Amin, Opt. Quant. Electron. 55 (6) (2023) 527.
[39] M. Ud Din, J. Munir, T. Alshahrani, H.I. Elsaeedy, Q. Ain, Mater. Sci. Semicond. Process. 163 (15) (2023) 107569.
[40] H. Murtaza, Q. Ain, J. Munir, H. M Ghaithan, A.A.A. Ahmed, A.S. Aldwayyan, S.M. H. Qaid, Phys. Scr. 99 (2024) 055947.
[41] M. Rani, P.K. Kamlesh, S. Kumawat, A.U. Rani, G. Arora, A.S. Verma, Phys. B Condens. Matter 680 (2024) 415645.
[42] A. Besbes, R. Djelti, I. Kars Durukan, Opt. Quant. Electron. 54 (372) (2022) 1–17.
[43] E. Haque, M.A. Hossain, Results Phys. 10 (2018) 458–465.